Simulation of abdominal MRI sequences in a computational 4D phantom for MRI-guided radiotherapy[A]

Paganelli C.[1], Summers P.[2], Bellomi M.[2,3], Baroni G.[1,4] and Riboldi M.[1]

[1]Dipartimento di Elettronica Informazione e Bioingegneria, Politecnico di Milano, Milano, Italy.
[2]Division of Radiology, Istituto Europeo di Oncologia, Milano, Italy.
[3]Department of Health Sciences, Università di Milano, Milano, Italy.
[4]Bioengineering Unit, Centro Nazionale di Adroterapia Oncologica, Pavia, Italy.

Abstract. A preliminary simulation of MRI sequences to derive a 4D MRI phantom for abdominal organs is presented, with the aim of providing a framework for the evaluation of MRI-guided methods in external beam radiotherapy. Specifically, we propose an extension of the 4D NCAT phantom including tissue parameters obtained via T1 and T2 DESPOT sequences, the simulation of dedicated abdominal MR sequences such as VIBE and TrueFISP, the modeling of radiofrequency coil response and noise followed by k-space sampling and image reconstruction. Analysis of tissue parameters and reconstructed images were performed to show the robustness of the implemented phantom.

Keywords. 4D MRI phantom, abdominal MRI, MRI reconstruction

1 Introduction

Over the last few years, there has been growing interest in the use of Magnetic Resonance Imaging (MRI) in image guided radiotherapy [1,2]. Due to the absence of ionizing radiation and increased soft tissue contrast relative to Computer Tomography (CT), MRI is an attractive technology for target definition [2]. Moreover, it has sufficient temporal resolution to study organ motion due to respiration [3]. Early studies investigating the use of MRI in treatment planning for organ motion quantification mainly followed cineMRI approaches [4,5], in which few slices are acquired allowing the description of a significant amount of breathing cycles. New four-dimensional MRI (4D MRI) retrospective sorting methods were also proposed to provide volumetric information of respiratory motion [6,7]. These features of MRI motivated also several recent technological developments towards the integration of MRI with radiation therapy treatment units, raising the prospect of fully MRI-guided treatments [8].

A standard approach to validation is the use of acquired in-vivo images as ground truth [9], which are not always available. In 4D MRI sorting, for example, a full resolu-

[A] **Acknowledgment:** The author would like to thank the Associazione Italiana per la Ricerca contro il Cancro (AIRC) for the support and Pifferi A. for the help during acquisitions.

tion 4D MRI cannot be obtained due to limited spatial and temporal trade-offs. Other solutions involve scanning MRI-compatible moving-structure phantoms [7,10], which do not often reflect the real internal anatomy. An MRI-compatible anthropomorphic moving phantom is under development [11], but the use of physical phantoms is generally limited due to their cost and the lack of flexibility to mimic the range of motions encountered in-vivo. Numerical digital phantoms offer a practical approach to evaluate and determine optimized methods. Examples have already been proposed for CT with the 4D cardiac-torso (NCAT) phantom, which incorporates natural beat-to-beat heart rate and respiratory motion variations, and then the extended (XCAT) version [12]. A number of MRI simulators have been developed, mainly for application to brain imaging, based on Bloch equations [13,14], but largely neglecting organ motion effects. The first implementations of numerical phantoms that incorporate motion in MRI for body radiotherapy were based on the extension of the 4D NCAT (and its extended XCAT version) by assigning MR properties to each tissue mask. Sharif et al. [15] proposed a physiologically improved NCAT (PINCAT) phantom in which the signal intensities were modified for MRI application to validate a dynamic MR imaging scheme in real-time cardiac MRI. In [16], a moving phantom was generated by segmenting cardiac images from an in-vivo acquisition by using a random affine transformation to simulate motion. However, in these cases a gray level to each tissue signal was also assigned, i.e. neglecting specific tissue properties. Wissmann et al. [17] designed a more realistic numerical phantom for cardiovascular MRI (MRXCAT) by extending the 4D XCAT phantom to MRI. They applied different tissue signal, multiple receiver coils and noise models, and selected arbitrary trajectories and undersampled acquisition of the k-space for accelerated cine and myocardial perfusion imaging, with specific cardiac MRI sequences.

In this work, we propose the basis for the construction of a 4D MRI phantom based on the 4D NCAT with an approach similar to the one proposed by Wissmann et al. [17] but extending the phantom to the abdominal site (abdoMRCAT) to account for organ motion due to respiration.

2 Materials and Methods

As proposed by Wissmann et al. [17], the phantom $P(\vec{k},t)$ is described in k-space through a combination of several weighting functions:

$$P(\vec{k},t) = R \cdot F \cdot [S(N_{coil}) \cdot T(T1,T2,\rho) \cdot C(TE,TR,\alpha) \cdot O(\vec{x},t) + n(\vec{x},t)]$$

where $O(\vec{x},t)$ represents the 4D NCAT phantom defined in space and time and $n(\vec{x},t)$ is the noise model. T is the tissue contribution as a function of relaxation times T1 and T2 and proton density ρ. The MR sequence is described by the operator C, which expresses the acquired signal as a function of repetition time TR, echo time TE and flip angle α. S describes the sensitivity of N_{coil} coils. These physical space functions undergo Fourier transformation F and the sampling of k-space R is applied to produce the raw k-space phantom $P(\vec{k},t)$. Once a complete k-space representation has been obtained, image reconstruction of the phantom can then follow via inverse Fourier transformation, as in the case of data sampled during image acquisition.

2.1 Tissue parameters T and MR sequences C

Two pulse sequences that are typically performed in abdominal MRI imaging were of interest for this study: (1) a T1-weighted spoiled volumetric interpolated breath-hold sequence (VIBE) [18] to acquire a 3D volumetric image in breath-hold and (2) a T2-weighted balanced steady-state free precession sequence (TrueFISP) [19] used during free-breathing to repeatedly acquire fast 2D images able to describe respiratory motion. Specifically at steady-state, the signal equations of the two different sequences C applied to each organ mask according to the specific relaxation times T1, T2 and proton density ρ values were as follows:

(1) VIBE: $C = \frac{\rho \sin\alpha(1-e^{\frac{-TR}{T1}})}{(1-\cos\alpha e^{\frac{-TR}{T1}})} e^{\frac{-TE}{T2}}$

(2) TrueFISP: $C = \rho \sin\alpha \frac{1-e^{\frac{-TR}{T1}}}{1-(e^{\frac{-TR}{T1}}-e^{\frac{-TR}{T2}})\cos\alpha - e^{\frac{-TR}{T1}} e^{\frac{-TR}{T2}}} e^{\frac{-TE}{T2}}$

The target sequence for in-vivo T1 and T2-weighted acquisitions (Fig. 1) used the following parameters (1.5T Siemens Magnetom Avanto):
- axial VIBE: TR/TE: 4.8msec/1.75msec; α: 68°; bandwidth: 601Hz per pixel; scan matrix: 256x224 pixels with spacing of 1.28x1.28mm; slice thickness of 5mm; acquisition time: 180msec/slice.
- sagittal TrueFISP: TR/TE: 2.9msec/1.26msec; α: 10°; bandwidth: 252Hz per pixel; percentage sampling: 70%; scan matrix: 240x320 pixels with spacing of 1.25x1.25mm; slice thickness of 4mm.

The imaging parameters of the acquired in-vivo images (TR, TE and α) were used in equations (1) and (2) for the generation of the abdoMRCAT images.
The dominant properties determining tissue appearance in MR imaging are T1 and T2 relaxation times and the proton density of the tissue. Proton density values ρ were not available for all abdominal organs in the literature [20], whereas relaxation times T1 and T2 were well defined in different works [21]. Therefore, in a first approach, an estimation of ρ (i.e. estimated ρ) was derived from in-vivo T1-weighted (i.e. VIBE) and T2-weighted (i.e. TrueFISP) acquisition, by segmenting a region of interest in each organ, and deriving ρ from the sequence equations (1) and (2) and performing a mean between the two ρ values. However, in order to avoid dependency from other factors (such as noise and potential artifacts), specific MRI sequences were acquired to estimate both T1, T2 and ρ values. Driven equilibrium single pulse observation of T1 (DESPOT1,11 flip angles in the range 3°-45°) and T2 (DESPOT2, 8 flip angles in the range 8°-64°) as described in [22] were acquired on the abdomen of one healthy volunteer. These acquisitions were used to derive T1-map, T2-map and ρ-map.
T1, T2 values were compared with the literature and ρ values derived from DESPOT acquisition were compared to the estimated values from equation (1) and (2) of in-vivo VIBE and TrueFISP (Wilcoxon test, alpha=5%). Differently from Wissmann et al. [17], no contrast agent concentration was considered.

2.2 Coil operator S and noise n

The effect of the coil sensitivity operator was implemented as proposed by [16], in which the phantom signal $(T(T1,T2,\rho)\cdot C(TE,TR,\alpha)\cdot O(\vec{x},t))$ was combined with a

simulated sensitivity map of the coil. The maps were designed as a linear fall-off with the sum of squares was equal to 1 and a circular arrangement of the coils around the abdomen (N_{coils}=8).
The presence of noise in MRI images was simulated by adding a Gaussian noise in order to satisfy the signal to noise ratio of in-vivo acquisitions (SNR=20).

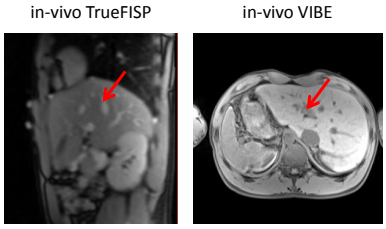

Fig. 1. In-vivo acquisitions. T2-weighted TrueFISP (left) and T1-weighted VIBE (right). Red arrows indicate blood.

2.3 k-space generation *F* and k-space sampling *R*

The image-domain model was transformed to the k-space domain via the discrete Fourier transform. Then, the k-space was sampled according to the sequence sampling approach. Specifically:
- VIBE [18]: the k-space was filled with a 70% sampling factor in the phase encoding (PE) directions. The remaining k-space was filled with zeros to provide smaller voxel size and maintain short imaging time.
- TrueFISP [19]: the k-space sampling was based on a generalized auto-calibrating partially parallel acquisition (GRAPPA) [23], with the aim to speed up the MRI pulse sequence in order to acquire fast slices able to describe the respiratory cycle(i.e. acquisition time ranged from 180msec to 300msec, as proposed in the literature [5]).
In the GRAPPA algorithm, unsampled k-space lines (i.e. sampling factor = 2, i.e. acquisition of interleaved lines) are synthesized by a linear combination of acquired neighboring k-space data (N_{FE}=256 and N_{PE}=256) using spatial information contained in the coil elements. The acquisition of additional lines in the k-space center is a form of self-calibration (i.e. auto-calibration (AC) lines, N_{ac}=16).

2.4 Image reconstruction

Once all k-space (3D for VIBE and 2D for TrueFISP) samples were obtained for a particular coil, an inverse Fourier transform was used to generate the uncombined image for that coil. The full set of N_{coils} uncombined images can then be combined using a normal sum of squares reconstruction [23].
Reconstructed images of all respiratory phases were qualitatively compared to in-vivo T1-weighted (VIBE) and T2-weighted (TrueFISP) acquisitions. Errors were quantified by computing the difference between the reference phantom and the reconstructed images.

3 Results

Table I shows the T1 and T2 values reported in the literature and ρ values derived from VIBE and TrueFISP equation (i.e. estimated ρ). In addition, T1, T2 and ρ values quantified via DESPOT acquisitions are also reported. Background and air were set to 0. Blood was not measured via DESPOT because of flow effects that cannot be compensated with the acquisition.T1 and T2 values derived from DESPOT differed from the literature [21] of 28% and 38% on average across tissues respectively, and the two populations (i.e. T1 and T2 literature vs. T1 and T2 DESPOT) did not result significantly different. The difference between ρ values derived from DESPOT and the ones estimated from VIBE and TrueFISP equations was as 37%. No significant difference was also observed between these two groups (i.e. estimated ρ vs. DESPOT ρ). Bowel, spleen and heart yielded higher estimated ρ values than the ones obtained with DESPOT. Values for ρ obtained with DESPOT for liver, spleen and bone were closer to literature ones [20] with respect to the estimated ρ.

Fig. 2 shows the abdoMRCAT images obtained by changing the proton density value of blood ρ_{blood} by using the estimated blood value from TrueFISP (12766) and VIBE (1397) separately and by using the mean of the two acquisitions (7081) for both sequences. A comparison with an in-vivo acquisition (Fig.1) shows that in the abdoMRCAT with a ρ_{blood} specific for each sequence, blood in the heart for the phantom resulted more similar to blood in vessels shown in in-vivo acquisitions (i.e. dark for VIBE and bright for TrueFISP) with respect to using the mean ρ_{blood} value (i.e. 7081) for both TrueFISP and VIBE simulations.

A quantitative analysis was also performed by computing the error as difference between the original phantom and the reconstructed one for all the respiratory phases (Fig. 3).The error maps showed pronounced edge effects for VIBE, whereas a more homogeneous distribution was maintained for TrueFISP. The errors obtained computing the difference between the original phantom and the reconstructed one were 10% and 7% (mean among all the phases) for VIBE and TrueFISP respectively.

Table 1. Tissue parameters. First and second columns: T1 and T2 values [msec] in the literature. Third column: estimated proton density ρ values [a.u.] from VIBE and TrueFISP acquisitions (literature values in brackets). Last columns: T1, T2 and ρ obtained from DESPOT maps.

	T1 [msec] literature	**T2 [msec] literature**	**estimated ρ (literature value) [a.u.]**	**T1 [msec] DESPOT**	**T2 [msec] DESPOT**	**ρ [a.u.] DESPOT**
background	0	0	0	0	0	0
air lung	0	0	0	0	0	0
body	240	85	1198	376	30	1336
bowel	100	10	1325	122	8	117
muscle	900	50	3342	825	28	3195
kidney	650	70	3832	921	40	1972
heart	1000	20	6150	1032	20	1346
liver	420	45	2797 (2182)	506	30	2023
blood	1500	20	7081	-	-	-
spleen	1514	65	4968 (2088)	1466	52	1428
cartilage	1060	35	977	588	16	1100
bone	732	30	916 (1343)	753	36	1041

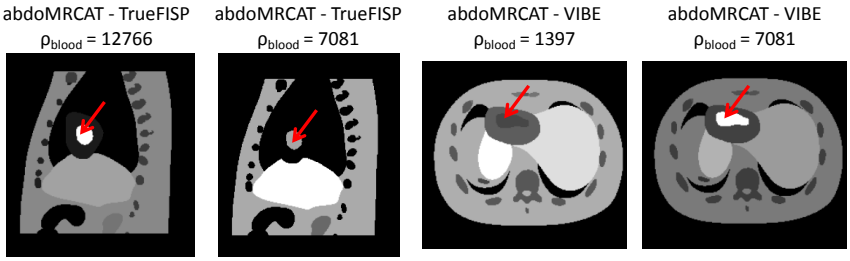

Fig. 2. Blood proton density. abdoMRCAT with a ρ_{blood} value selected in a sequence-specific fashion (i.e. 12766 for TrueFISP and 1397 for VIBE) and a mean value approach (7081) for both sequences. Red arrows indicate blood.

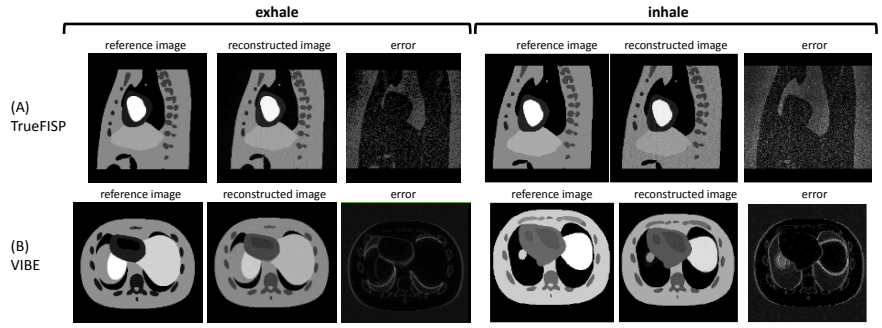

Fig. 3. Image reconstruction. (A) TrueFISP and (B) VIBE with the original reference MRI phantom, the reconstructed image and the error for both exhale and inhale.

4 Discussion and Conclusion

In this work, we describe the basis for the implementation of an abdominal 4D MRI phantom by extending the 4D NCAT phantom designed by Segars et al. [12]. A similar work has previously been reported in the literature by Wissmann et al. [17] for cardiac acquisitions. Our aim was to provide a phantom able to describe respiratory motion of abdominal organs in MRI that can be used for validation purposes.

The tissue parameters T1 and T2 obtained using specific MR sequences (i.e. DESPOT1 and DESPOT2) [22] were consistent with the literature [21], supporting their use in the phantom. Our acquisitions did not however take into account inhomogeneities which are recognized to influence T1 and T2 measurement. Subtle corrections in the T1 and T2 values may therefore be warranted in the future. Proton density values for abdominal organs appear to be largely absent from the literature. The values obtained from ρ-maps derived from the DESPOT data were compared with estimated values extracted from in-vivo T1-weighted and T2-weighted acquisitions (i.e. deriving ρ values from equation (1) and (2)): a mean discrepancy of 37% was found, with comparable values in all organs, without a significant difference between estimated ρ and DESPOT ρ. Spleen, bowel and heart ρ values were over-estimated by in-vivo T1/T2

acquisitions (4968). However for spleen, a lower value was observed in DESPOT (1428) resulting more similar to the literature (2088). Also bowel and heart presented lower values in DESPOT estimation, however these two organs were difficult to analyze due to artifacts associated with filling and contraction. Furthermore, we did not derive the proton density value for blood as flow effects [24] could not be adequately compensated for with the available DESPOT sequences, and in the presence of in/out-flowing blood, the signal equations (i.e. equation (1) and (2)) are not appropriate for the VIBE and TrueFISP signals. Moreover, the magnetization described by the signal equations does not include signal alteration due to motion during sampling [17]. In addition, steady-state free precession MRI as TrueFISP is a type of gradient echo MRI pulse sequence in which a steady, residual transverse magnetization is maintained between adjacent breathing cycles. Conversely, spoiled gradient echo MRI, such as VIBE, is an MRI technique which destroys residual transverse magnetization at the end of each excitation cycle. Blood and other fluids may therefore exhibit spoiled contrast behavior, even though stationary tissue remains in a steady-state free precession. For this purpose, in order to obtain simulations similar to in-vivo acquisitions, we applied to blood the specific estimated ρ value obtained via in-vivo T1 and T2-weighted acquisitions, allowing to have dark blood and bright blood in VIBE and TrueFISP respectively, even if blood flow is not adequately accounted for by their signal equations. In addition, the reconstruction errors were 10% and 7% for VIBE and TrueFISP respectively, with more errors along the edges being present in the VIBE reconstruction (Fig. 3) due to a central sampling of the k-space and to a volumetric interpolation in contrast to the calibrated and bi-dimensional reconstruction of the TrueFISP acquisition.

In conclusion, we presented the preliminary steps on the simulation of MRI sequences for the construction of an abdominal 4D MRI phantom that can be considered as a framework for the validation of MR image reconstruction and quantitative post-processing approaches to improve organ motion quantification and compensation. Furthermore, our work provided also a preliminary quantification of tissue parameters including proton density values of abdominal organs. Future works on tissue parameters are needed as MR-based measurements are dependent on sequence used and sources of error such as field inhomogeneity. Because a spin's history of radio-frequency pulses and relaxation intervals determines the appearance in MRI, a more extensive consideration of the object model is required in MR simulations. In addition, a deep analysis of the reconstruction effects on the 4D motion will be taken into consideration. Further extensions to the phantom include the incorporation of spin history and additional effects such as susceptibility and magnetization transfer.

5 References

1. Hugo G D, Rosu M. Advances in 4D radiation therapy for managing respiration: Part I – 4D imaging. Med Phys; 22:258–271 (2012)
2. Metcalfe P, Liney GP, Holloway L et al. The Potential for an Enhanced Role For MRI in Radiation-therapy Treatment Planning Technology in Cancer Research & Treatment; 1-18 (2013)
3. Biederer J, Hintze C, Fabel M, Dinkel J. Magnetic Resonance Imaging and Computed Tomography of Respiratory Mechanics. Journal of Magnetic Resonance Imaging; 32:1388–1397 (2010)

4. Sawant A, Keall P, Pauly KB, et al. Investigating the feasibility of rapid MRI for image-guided motion management in lung cancer radiotherapy. BioMed Res Int;2014:48506 (2014)
5. Paganelli C, Seregni M., Fattori G. et al. Magnetic Resonance Imaging Guided versus Surrogate-Based Motion Tracking in Liver Radiation Therapy: A Prospective Comparative Study, Int J Radiation Oncol Biol Phys; 91: 840-848 (2015)
6. vonSiebenthal M, Székely G, Gamper U et al. 4D MR imaging of respiratory organ motion and its variability. Phys Med Biol;52:1547–1564 (2007)
7. Cai J, Chang Z, Wang ZH et al. Four-dimensional magnetic resonance imaging (4D-MRI) using image-based respiratory surrogate: A feasibility study. Med Phys;38:63-84 (2011)
8. Keall PJ, Barton M, Crozier S. The Australian magnetic resonance imaging-linac program. Semin Radiat Oncol;24:203-206 (2014)
9. Weon C, Nam WH, Lee D, et al. Position tracking of moving liver lesion based on real-time registration between 2D ultrasound and 3D preoperative images, Medical physics, 42: 335-345(2015)
10. http://modusmed.com/qa-phantoms/mri-respiratory-motion
11. Perrin R, Peroni M, Bernatowicz K et al. A Realistic Breathing Phantom of the Thorax for Testing New Motion Mitigation Techniques with Scanning Proton Therapy. Med. Phys. 41, 111 (2014)
12. Segars PW, Sturgeon G et al. 4D XCAT phantom for multimodality imaging research. Med. Phys; 37: 4902-4915 (2010)
13. http://mrilab.sourceforge.net/
14. Benoit-Cattin H, Collewet G et al. The SIMRI project: a versatile and interactive MRI simulator. Journal of Magnetic Resonance 173: 97–115 (2005)
15. Sharif B and Bresler Y. Adaptive real-time cardiac MRI using PARADISE: validation by the physiologically improved NCAT phantom. Proc IEEE Int Symp Biomed Imaging (2014)
16. Aja-Fernandez S, Cordero-Grande L et al. A MRI phantom for cardiac perfusion simulation. IEEE ISBI (2012)
17. Wissmann L, Santelli C, Segars WP, Kozerke S. MRXCAT: Realistic Numerical Phantoms for Cardiovascular Magnetic Resonance. J Cardiovasc Magn Reson;16:63 (2014)
18. Rofsky NM, Lee VS et al. Abdominal MR Imaging with a Volumetric Interpolated Breath-hold Examination. Radiology, (1999)
19. Fuchs F, Laub G et al. TrueFISP: technical considerations and cardiovascular applications. European Journal of Radiology 46: 23-32 (2003)
20. Nyman R, Ericsson A, et al. T1, T2, and relative proton density at 0.35 T for spleen, liver, adipose tissue, and vertebral body: normal values. Magn Reson Med.;3(6):901-10 (1986)
21. Bernstein MA, King KF, Zhou XJ: Basic pulse sequences. Handbook of MRI Pulse Sequences (2004)
22. Deoni SCL, Rutt BK et al. Rapid Combined T1 and T2 Mapping Using Gradient Recalled Acquisition in the Steady State. Magnetic Resonance in Medicine 49:515–526 (2003)
23. Griswold M A, Jakob P M, et al. Generalized Autocalibrating Partially Parallel Acquisitions (GRAPPA). Magnetic Resonance in Medicine 47:1202–1210 (2002)
24. Axel L. Blood flow effects in magnetic resonance imaging. Magn Reson Annu. 237-44 (1986)